

Surface-to-Volume Ratio of Porous Materials Obtained by a Combined Use of NMR and MIP

E. W. Hansen,^{*,†} H. C. Gran,^{‡,§} P. O. Kvernberg,[§] and B. Pedersen[§]

SINTEF Applied Chemistry, P.O. Box 124 Blindern, 0314 Oslo, Norway, Norwegian Building Research Institute, P.O. Box 123 Blindern, 0314 Oslo, Norway, and Department of Chemistry, University of Oslo, P.O. Box 1033, Blindern, 0315 Oslo, Norway

Received: June 12, 1997; In Final Form: August 27, 1997[®]

Porous materials are characterized by a finite and discrete number of pore radii by deconvoluting the respective mercury intrusion porosimetry (MIP) curves. Introducing a perturbed cylindrical pore model enables these MIP radii to be correlated to the NMR spin–lattice relaxation time T_1 of the pore-confined water to give the surface-to-volume ratio (S/V) of the pores. The technique is exemplified using four different well-hydrated white Portland cement pastes covering a wide distribution of pore sizes. However, the technique should be of general use when characterizing high surface-to-volume ratio materials.

Introduction

Measurement of the ^1H NMR spin–lattice relaxation time, T_1 , and spin–spin relaxation time, T_2 , have been demonstrated as important tools in the characterization of pore size distributions of various porous materials. The technique is a valuable supplement to other principal techniques such as mercury intrusion porosimetry (MIP), gas adsorption/desorption, low-angle X-ray scattering, and optical/electron microscopy. In contrast to other techniques, NMR is nondestructive and does not require any kind of drying or vacuum treatment before testing. Drying or evacuation may cause artificial changes to the structure of some materials. Pore size distributions derived from NMR are based on well-established correlations between relaxation times T_1 and T_2 of the pore-confined liquid and the surface-to-volume ratio of the pore system.^{1,2} For spherical and cylindrical pore geometries, these relations can be shown to be proportional to the inverse pore radius.

Several workers have compared the spin–lattice and spin–spin relaxation times to pore size distributions observed with MIP. However, a majority of the reported measurements found in the literature have been performed on porous materials with simplified pore systems and narrow pore size distributions such as zeolites, different leached glasses, and packed spheres.^{2–7} In general, a linear relationship between NMR relaxation time data and MIP data has been found for wider pores, whereas smaller pore radii pose problems, possibly due to breakdown of the model predicting linearity between relaxation time and pore radius determined by MIP. An explanation for this is the inaccessibility of the finer structures of the pore system to mercury. Bhattacharja et al.⁵ chose to use a surface relaxation parameter based on surfaces determined by nitrogen adsorption in their NMR pore size measurements. Gallegos et al.⁴ concluded that an assumption or correction concerning pore geometry or surface layer volume was required.

In this work, NMR spin–lattice relaxation data and pore sizes measured by MIP are presented using materials with a wide distribution of pore sizes and with uniform surface chemistry. For this purpose four different well-hydrated white Portland

cement pastes were selected. A particular characteristic of hydrated cement pastes is a distribution of pore sizes from a few angstroms to several tens of micrometers. The distribution of pore sizes is mainly determined by the ratio of mixing between water and cement when the cement paste is produced. At water/cement ratios below about 0.40 the pore system is dominated by micro- and mesopores which are intrinsic to the hydrated cement gel. At higher water/cement ratios capillary pores appear resulting from excess water that is not directly taking part in the cement hydration.⁸

The object of the present work is to combine MIP and NMR spin–lattice relaxation time measurements to derive the overall surface-to-volume (S/V) ratio of porous materials. Although the pore dimensions derived from the two methods will be basically different, we will show that the two different experimental techniques can be combined to predict the S/V ratio by introducing a perturbation of the assumed cylindrical pore geometry.

The method of perturbing an ideal pore geometry (cylindrical, spherical) will have general applicability when aiming at deriving the S/V ratio of porous materials from a combined use of NMR and MIP.

Experimental Section

Materials. Samples of hydrated cement paste (HCP) with three different mix weight ratios between water (w) and cement (c) were used in the experiments. The mix ratios between water and cement were $w/c = 0.40$ (sample S04), 0.60 (sample S06), 0.70 (sample S07), and 1.0 (sample S10). All pastes were made from a Danish Super White Portland Cement certified as a British Standards Institution class 62.5N cement, with a Bogue composition of 65.8% tricalcium silicate (C_3S), 21.0% dicalcium silicate (C_2S), 4.18% tricalcium aluminate (C_3A), 0.96% tetra-calcium alumina ferrite (C_4AF), and 2.32% calcium oxide (C) and a Blaine surface of 4000 cm^2/g . The reason for using a white cement was its low content of paramagnetic constituents such as Fe_2O_3 and Mn_2O_3 that may contribute to the NMR relaxation.⁶ The composition by weight of the cement was determined by X-ray fluorescence spectroscopy at the laboratory of Aalborg Portland; see Table 1. The pastes were mixed under slight vacuum (0.1 bar to 10 kPa) to avoid entrapped air, molded, and sealed in cylindrical polytetrafluoroethane forms with a diameter of 20 mm and a length of 120 mm. The total weights

* To whom correspondence should be addressed.

† SINTEF Applied Chemistry.

‡ Norwegian Building Research Institute.

§ University of Oslo.

® Abstract published in *Advance ACS Abstracts*, October 15, 1997.

TABLE 1: Composition of White Portland Cement Given as Percent by Weight of Oxide Compared to the Total Amount of Cement

oxide	% by weight
SiO ₂	24.0
CaO	71.0
Al ₂ O ₃	2.10
Fe ₂ O ₃	0.31
MnO	0.012
MgO	0.55
K ₂ O	0.04
Na ₂ O	0.14
SO ₃	1.23
loss on ignition	0.67

of the mixtures were checked before and after mixing to detect any loss of water resulting from the vacuum treatment. The pastes were slowly rotated during the first 20 h of hardening to avoid separation between water and cement. After demolding, the H₂O paste was stored in water at room temperature. The samples were 3 months old at the time of testing. Parallel samples were taken for MIP and NMR measurements. The samples were cut from the interior of the molded cylinders to avoid possible inhomogeneities in the paste caused by the proximity to the form walls.

MIP. The MIP measurements were performed on a Carlo Erba Strumentazione 2000 porosimeter capable of producing pressures up to 2000 bar. Samples were outgassed for 2 h to less than 3 mbar in the dilatometer cell before inlet of the mercury. After the mercury had entered the cell, atmospheric pressure was established and counteradjusted to 1 bar. Intrusion caused by atmospheric pressure was less than 0.1% of the specimen volume and has not been accounted for. Pore radii were determined from the Washburn equation⁹ assuming a contact angle of 117° and a surface tension of 480 dyn/cm² (48 Pa).¹⁰ Samples of cement paste were cut and ground to a cylindrical shape diameter of 12 mm and length of 40 mm.

NMR. Spin-lattice relaxation times were measured on a Bruker CXP 200 NMR instrument, operating at 200 MHz proton resonance frequency. All measurements were performed using a conventional inversion recovery (180°-τ-90°) pulse sequence. The delay time, τ, between the initial 180° pulse and the 90° read pulse was varied between 100 μs and 12 s. Each observed decay curve was characterized by 78 different τ values. The applied 90° pulse length was 6.0 μs with a pulse repetition time of 12.5 s. The bandwidth was set to 100 kHz using an acquisition time of 0.082 s. A total of 16 transients were accumulated at each τ value. The samples of hydrated cement paste were cut and ground to a diameter of 3.5 mm and a length of 10 mm and stored in small amounts of distilled water. Four days before testing they were outgassed for 3 h—as for the MIP samples—and resaturated with distilled water. Immediately before testing the water on the external surface was wiped away with an absorbent tissue before being transferred to the 5 mm NMR tube. Each tube was finally sealed with a plastic cap covered with epoxy to prevent water vapor escaping from the sample. The sample weight was checked immediately before and after the experiment.

Results and Discussion

To characterize the porous network of the cement paste, the volume of intruded mercury, *I*, vs inverse pore dimension, 1/*R*, was measured by MIP. The results are plotted in Figure 1. 1/*R* was determined by applying the Washburn equation,⁹ which relates pressure to pore dimension under the assumption of cylindrical pore geometry. The lack of any sharp, abrupt change in *I* vs 1/*R* suggests that a distribution of pore sizes exists. To

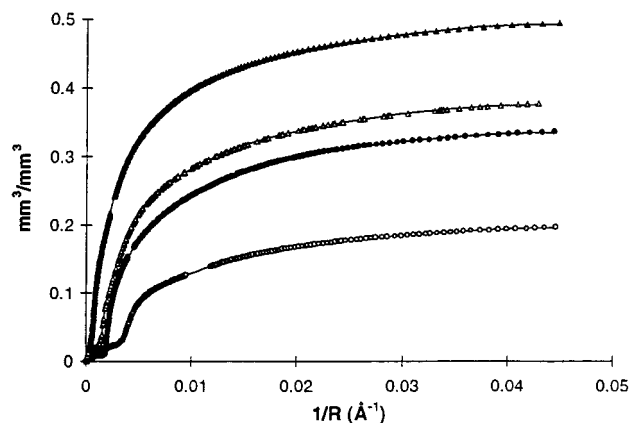


Figure 1. Mercury intrusion curves (MIP) for samples S04 (○), S06 (●), S07 (△), and S10 (▲), showing intruded volume vs inverse pore radius. The solid curves represent least-squares fits of eq 1 (*N* = 6) to the observed data points.

determine this distribution, we have assumed that it can be approximated by a finite number (*N*) of Gaussian functions, centered at 1/*R_i* (*i* = 1 – *N*) and having a width at half-height equal to Δ_{*i*}.

The amount of mercury, *I*, within pores of radius *R* ≥ *R*₀ can be expressed by the function

$$I(1/R_0) = \frac{1}{\sqrt{\pi}} \sum_{i=1}^N I_{0i} \int_{\frac{1/R_0 - 1/R_i}{\sqrt{2}\sigma_i}}^{\frac{1/R_0 - 1/R_i}{\sqrt{2}\sigma_i}} \exp(-u^2) du \quad (1)$$

where *N* defines the number of discrete pore sizes needed to fit the MIP curve. *N* was determined to be equal to 6 (Table 2)—for all four samples investigated—by carrying out statistical validity tests (f-tests).

The solid curves in Figure 1 represent nonlinear least-squares fit of eq 1 to the observed data. The numerical values are summarized in Table 2.

If the diffusion of water molecules within the six pore domains (MIP) is fast on an NMR time scale and slow between the six domains, the NMR measurement would be expected to give six different spin-lattice relaxation times. As will be seen below, this is not the case. Figure 2 shows the NMR spin-lattice relaxation curves (longitudinal magnetization vs inter pulse timing, τ) for the four samples investigated in this work. For a discrete number (*N*) of spin-lattice relaxation times, *T*_{1*i*} (*i* = 1, *N*), the relaxation curve can be written as a sum of exponential curves as given by eq 2,

$$M = \sum_{i=1}^N M_{0i} (1 + \alpha \exp(-\tau/T_{1i})) \quad (2)$$

corresponding to *N* separate groups of protons (water molecules) with different relaxation rates. *M*_{0*i*} represents the equilibrium magnetization of component *i*, and α is an adjustable parameter which in this case takes account of inhomogeneities in the rf pulse. In general, α is expressed by α = (2Σ_{*j*=1}^{*m*} cos Θ_{*j*})/*m*, where *m* is the number of spins disturbed by the rf pulse and Θ_{*j*} is the pulse angle of the *j*th spin. For perfect pulses, Θ_{*j*} is 180° for all spins, implying that α = –2.

It was found that the decay curves were best fitted to a sum of two exponentials, which has also been reported for *T*₂ measurements by Bhattacharja et al.⁷ The solid curves in Figure 2 represent nonlinear least-squares fits of eq 2 to the observed relaxation data. The results are summarized in Table 3. Fitting

TABLE 2: Pore Size Distribution of Samples S04, S06, S07, and S10 Approximated by a Discrete and Finite Number $N (=6)$ of Gaussian Functions with Relative Volume Contribution I_i , Mean Average Inverse Pore Size $1/R_i$, and Width Δ_i^a

sample	parameter	i						r^2
		1	2	3	4	5	6	
S04	I_i	0.00847	0.00896	0.0312	0.0356	0.0413	0.0410	0.999974
	$\sigma(I_i)$	0.00064	0.0020	0.0013	0.0036	0.025	0.033	
	$1/R_i$	0.000836	0.001372	0.004020	0.004724	0.007285	0.01385	
	$\sigma(1/R_i)$	6.8×10^{-6}	7.9×10^{-5}	4.7×10^{-6}	5.4×10^{-5}	3.3×10^{-4}	0.0029	
	Δ_i	0.000150	0.000670	0.000370	0.000980	0.003342	0.005825	
S06	I_i	0.0437	0.0421	0.0497	0.0683	0.0794	0.0539	0.999953
	$\sigma(I_i)$	0.0025	0.0068	0.0082	0.0096	0.017	0.011	
	$1/R_i$	0.002091	0.002504	0.003426	0.005387	0.010820	0.023600	
	$\sigma(1/R_i)$	1.5×10^{-6}	2.6×10^{-5}	0.00011	0.00016	0.00051	0.0025	
	Δ_i	0.000116	0.000329	0.000812	0.002231	0.005235	0.010920	
S07	I_i	45.8	172	423	377	335	326	0.999948
	$\sigma(I_i)$	5.5	8.6	141	225	169	88	
	$1/R_i$	0.000181	0.001167	0.002538	0.0044	0.009114	0.020903	
	$\sigma(1/R_i)$	1.1×10^{-5}	4.9×10^{-6}	3.4×10^{-5}	7.9×10^{-4}	0.0015	0.0030	
	Δ_i	0.000062	0.000158	0.000894	0.001818	0.004462	0.010182	
S10	I_i	0.105	0.098	0.096	0.076	0.064	0.054	0.999944
	$\sigma(I_i)$	0.0033	0.106	0.149	0.084	0.061	0.028	
	$1/R_i$	0.000778	0.001579	0.003008	0.005917	0.011811	0.024614	
	$\sigma(1/R_i)$	3.7×10^{-6}	1.2×10^{-4}	0.0013	0.0017	0.0031	0.0054	
	Δ_i	0.000295	0.000852	0.001278	0.002462	0.004868	0.009887	

^a The uncertainty is denoted by σ , which is the normal standard deviation. the numerical data are obtained by fitting eq 5 to the observed MIP curves (Figure 2). The correlation coefficients are given by r^2 . See text for further details.

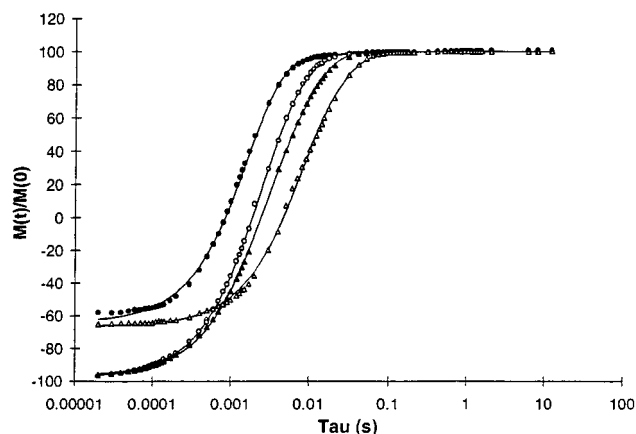


Figure 2. NMR magnetization decay curves for sample S04 (●), S06 (○), S07 (△), and S10 (△). The solid curves represent least-squares fits using a sum of two exponential functions as given by eq 2.

the relaxation curve by more than two exponentials did not improve the fit as confirmed by statistical validity tests (f-tests).

The observation that water confined in the four cement pastes is characterized by two relaxation rates and not six (MIP) must be related to the fact that relaxation measurements are weighted by diffusion and that the diffusion of water molecules between some of the pore domains is fast on an NMR time scale. This observation is in accordance with the diffusion cell model discussed by Halperin et al.¹¹ The reason for observing two different NMR relaxation times is that two poorly diffusional communicating domains within the cement paste exist. This does not mean that the two pore systems are isolated from each other, but simply that the exchange of water between them is slow on the NMR time scale. This might for instance originate from narrow pore coupling between the two pore domains causing a diffusion-limited exchange of water between them. However, each of the two pore domains might be composed of more than one "pore" size, with an exchange of water between them which is fast on the NMR time scale.

The simplest physical model describing systems in fast exchange is the "two-fraction fast exchange" model of Zimmerman and Brittin.¹² The model assumes two magnetically distinct systems or phases: a bulk phase with a relaxation time,

$T_{1,B}$, which is characteristic of bulk liquid and a phase close to the pore surface with a much shorter relaxation time, $T_{1,S}$. The observed spin-lattice relaxation rate $1/T_1$ can be expressed by

$$\frac{1}{T_1} = \frac{f}{T_{1,B}} + \frac{1-f}{T_{1,S}} \quad (3)$$

where f represents the mole fraction of "bulk" water and may be written

$$f = 1 - \frac{\lambda S}{V} \quad (4)$$

where λ is the thickness of the surface layer close to the pore wall, V is the volume, and S is the surface area of the pore. λ is assumed to be constant.

From these theoretical considerations^{2,4} the relaxation rate can be related to the surface-to-volume ratio (S/V) by combining eqs 3 and 4:

$$\frac{1}{T_1} = \frac{1}{T_{1,B}} + \left(\frac{1}{T_{1,S}} - \frac{1}{T_{1,B}} \right) \lambda \frac{S}{V} \quad (5)$$

Equation 5 shows that the observed spin-lattice relaxation rate is expected to be proportional to the surface-to-volume ratio times the thickness of the water surface layer. If assuming cylindrical pores with radius R , the surface-to-volume ratio can be replaced by $2/R$, suggesting the spin-lattice relaxation rate to be proportional to the inverse pore radius.

As can be concluded from the MIP and NMR measurements, the two methods give significantly different results regarding pore dimensions, which is not unexpected since each different method measures something different about the porous material. However, the combined information gained from the two techniques can be combined to extract the overall S/V ratio of the samples investigated. To perform this, we will (1) contract the six cylindrical pore geometries obtained from MIP into two pore systems under the constraint of volume conservation and (2) combine these two pore systems with the two corresponding sets of spin-lattice relaxation data from NMR. We will assume that these two-pore systems can be—basically—approximated by cylindrical pore geometries in accordance with MIP-derived

TABLE 3: Relaxation Times $T_{1,I}$ and $T_{1,II}$, Relative Volumes V_I and V_{II} , and Volume Ratios V_I/V_{II} Derived from NMR Measurements for Samples S04, S06, S07, and S10; Uncertainties Are Given as Standard Deviation, while 95% Confidence Intervals Are Shown in Parentheses

sample	$T_{1,I}$ (ms)	V_I	$T_{1,II}$ (ms)	V_{II}	$(V_I/V_{II})_{\text{NMR}}$
S04	1.50 ± 0.22 (0.51)	105.3 ± 1.4 (2.8)	8.58 ± 1.29 (3.0)	8.8 ± 1.4 (2.8)	11.9 ± 1.9 (4.8)
S06	1.92 ± 0.056 (0.13)	62.9 ± 3.1 (6.2)	5.41 ± 0.21 (0.48)	42.1 ± 3.1 (6.2)	1.49 ± 0.13 (0.39)
S07	2.0 ± 0.044 (0.10)	16.6 ± 0.46 (0.92)	7.7 ± 0.15 (0.35)	16.7 ± 0.46 (0.92)	0.994 ± 0.04 (0.12)
S10	6.85 ± 0.32 (0.74)	71.6 ± 11.7 (23.4)	19.5 ± 1.2 (2.8)	67.0 ± 11.7 (23.4)	1.07 ± 0.26 (0.78)

geometries. Due to the size of the probe molecule (Hg) used in MIP, this technique will not be able to detect the smaller pores ($R < 10\text{--}20 \text{ \AA}$). This means that the volumes derived from MIP might be smaller than the volumes observed by NMR (water used as a probe molecule) and needs to be taken into account when comparing the two different experimental techniques. We will resolve this by perturbing the pure cylindrical pore geometry. The choice of such a perturbation function is somewhat arbitrary and will mainly be dictated by the mathematical complexity. We believe, however, that the choice of perturbation function will not be very sensitive to the outcome of the analysis.

Before proceeding further some comments regarding the potential loss of signal intensity due to a fast transverse relaxation (T_2^* effects) in combination with “long” dead times (time elapsed before sampling the NMR signal) of $10 \mu\text{s}$ need to be addressed. Preliminary work (not published) has shown that the observed signal intensity for fully water saturated samples is directly proportional to the amount of mobile or evaporable water confined in the pores (testing cement pastes with different porosities). However, for partly saturated water samples (20–30%) this linearity breaks down. The reason, we believe, is that the fast exchange conditions are not met (see previous discussion in this section). For the fully saturated samples investigated in this work, we believe that the fast exchange conditions are fulfilled and that problems related to dead times will be of marginal relevance to this work.

Averaging of Pore Sizes Derived from MIP Measurements. If a finite number (M) of cylindrical pores are connected in such a way that the confined water satisfies the fast exchange condition, the overall and observable relaxation rate ($1/T_1$) can be described by a generalized version of eq 5, i.e.,

$$\frac{1}{T_1} = \frac{1}{T_{1B}} + \frac{2\lambda}{T_{1S}} \sum_{i=1}^M \frac{V_i}{V_0} \frac{1}{R_i} \quad (6a)$$

where R_i and V_i are the pore radius and pore volume of the individual cylindrical pores. It follows from eq 6a that the average pore radius of the M connected pores can be defined by the second term on the right side of this equation, i.e.,

$$\frac{1}{R} = \sum_{i=1}^M \left(\frac{V_i}{V_0} \right) \frac{1}{R_i} \quad (6b)$$

where $V_0 = \sum_{i=1}^M V_i$. The question then arises of how to combine the previously determined six pore radii into only two pore radii. Combinatorial statistics tells us that this can be performed in 31 ways

$$= \frac{1^{n=5}}{2} \sum_{n=1}^5 \frac{6!}{n!(6-n)!}$$

The 31 possible combinations are shown in Table 4 for each of the four samples, where the notations I and II have been used to differentiate between the two contracted pore systems.

For simplicity the symbol I is used for the smaller pores, i.e., $R_I < R_{II}$. The corresponding volumes are denoted V_I and V_{II} .

As can be discerned from Table 4, the 31 sets of paired pore combinations (I, II) display a large spread in pore sizes (R_I , R_{II}). Since we are aiming at finding a single solution of paired pore radii for each of the four samples, some reasonable strategy has to be encountered. Before discussing this subject in more detail we will first consider the pore model concept.

Pore Model. The MIP technique implicitly assumes that the pores are cylindrical in shape. As already mentioned, NMR cannot differentiate between pores that are connected in such a way that diffusion of confined fluid is fast on an NMR time scale. Thus, the mathematical contraction of six to two pores from MIP (using eq 6b) cannot be expected to give a cylindrical pore shape. Moreover, due to the larger volume of the Hg molecule compared to the water molecule, the former cannot enter the micropores of the cement paste, suggesting that these pore volumes are undetectable by MIP. This will inevitably lead to an underestimate of the pore volume determined by MIP as compared to NMR. We will show that when introducing a simple perturbation of the assumed cylindrical pore geometry, these differences can be rationalized and used to advantage.

Two simple ways of mathematically perturbing the pure cylindrical geometry is (1) to modify the circular base of the pore cylinder or/and (2) to modify the surface of the pore cylinder wall. We have tested both types of modulations and found that the latter technique results in a somewhat more simplified mathematical procedure. In this work we will thus only pay attention to this latter modification of the pore geometry. Details concerning the derivation of the formulas presented in this section are discussed more thoroughly in the Appendix.

We perturb the surface of the pore wall by a cosine function of the form

$$R = R_0 + \Delta \left[1 + \cos\left(\frac{\pi z}{L}\right) \right] \quad (7)$$

where R_0 is the radius of the unperturbed cylindrical surface, i.e., the radius determined from MIP. L represents the half-width of the pore opening along the z -axis, and Δ is the amplitude of the perturbation. This situation is illustrated schematically in Figure 3, which shows a three-dimensional (A) and a two-dimensional (B) picture of the pore. The total volume (V) of one segment of the perturbed cylinder (shaded area in Figure 3) can be shown to be (see Appendix)

$$V = \pi R_0^2 L + \frac{1}{2} \pi L \Delta (4R_0 + 3\Delta) \quad (8a)$$

Since the volume on the left side can be identified with the volume determined by NMR and $\pi R_0^2 L$ can be identified with the volume of the pore defined by MIP, eq 8a can be reformulated to read

$$V_{\text{NMR}} = V_{\text{MIP}} \left[1 + 2 \frac{\Delta}{R_0} + \frac{3}{2} \left(\frac{\Delta}{R_0} \right)^2 \right] \quad (8b)$$

TABLE 4: Pore Radii (R_I and R_{II}) and Pore Volume Ratios F_{MIP} ($=V_I/V_{II}$)_{MIP} Calculated by Contracting the Number of Discrete Pore Radii Measured with MIP from Six to Two (I and II) Using Eq 6b^a

<i>n</i>	pore system (I)	pore system (II)	S04		S06		S07		S10	
			R_I/R_{II}	F_{MIP}	R_I/R_{II}	F_{MIP}	R_I/R_{II}	F_{MIP}	R_I/R_{II}	F_{MIP}
1	1	2,3,4,5,6	135/1197	4.9*	106/478	0.6*	127/5391	7	130/1286	2*
2	1,2	3,4,5,6	128/900	2.4	94/436	0.3	116/737	1.5*	103/860	0.90*
3	1,3	2,4,5,6	121/299	1.1	94/357	0.3	102/144	0.6*	108/543	0.75*
4	1,4	2,3,5,6	122/251	0.9	94/244	0.21	112/254	0.56*	123/340	1.1*
5	1,5	2,3,4,6	134/162	0.7	112/129	0.15	124/132	1.4*	145/203	1.2*
6	1,6	2,3,4,5	861/193	1.9	72/159	4.3	55/215	1.2*	112/203	4.3
7	1,2,3	4,5,6	114/336	0.9	81/369	0.17	90/468	0.46*	76/570	0.36*
8	1,2,4	3,5,6	114/283	0.8	80/273	0.15	99/304	0.40	90/406	0.58*
9	1,2,5	3,4,6	125/183	0.6	95/156	0.10	118/165	0.51*	109/270	0.65*
10	1,2,6	3,4,5	100/182	2.3	95/141	6.5	77/196	1.7	158/163	6.5
11	1,3,4	2,5,6	104/250	0.6	78/257	0.13	82/309	0.23	96/337	0.45*
12	1,3,5	2,4,6	114/187	0.4	94/154	0.09	100/194	0.30	118/236	0.52*
13	1,3,6	2,4,5	115/178	3.1	96/142	7.0	101/177	2.8	150/175	7.0
14	1,4,5	2,3,6	115/179	0.4	94/145	0.08	113/161	0.22	139/191	0.75*
15	1,4,6	2,3,5	115/186	3.3	96/151	8.2	88/211	3.4	126/216	8.2
16	1,5,6	2,3,4	104/248	21	80/249	12.3	72/322	2.7	103/302	12.3
17	1,2,3,4	5,6	95/269	0.5	63/277	0.10	67/336	0.19	56/384	0.18*
18	1,2,3,5	4,6	104/202	0.4	75/175	0.07	83/221	0.25	73/284	0.25*
19	1,2,3,6	4,5	126/164	3.5*	116/120	9.6	118/151	3.4	116/190	9.6
20	1,2,4,5	3,6	104/193	0.3	72/164	0.06	95/186	0.18	92/238	0.44*
21	1,2,4,6	3,5	125/170	3.7*	113/125	10.9	105/184	4.2	154/165	10.9
22	1,2,5,6	3,4	112/228	26	94/219	17.3	87/293	3.3	138/233	17.3
23	1,3,4,5	2,6	86/194	0.3	70/162	0.06	70/204	0.075	102/217	0.32*
24	1,3,4,6	2,5	134/160	4.6*	113/126	11.6	123/152	6.9	154/178	11.6
25	1,3,5,6	2,4	122/247	30	95/233	19.3	103/282	5.0	130/287	19.3
26	1,4,5,6	2,3	121/292	54	95/333	23.0	94/438	7.7	114/437	23.0
27	1,3,4,5,6	2	135/729	81	107/399	43.3	120/600	1.76	136/633	43.3
28	1,2,4,5,6	3	128/249	105	107/292	34.9	106/394	8.9	143/332	34.9
29	1,2,3,5,6	4	129/212	36	108/186	28.0	116/227	5.8	160/169	28.0
30	1,2,3,4,6	5	137/142	0.2	92/128	0.067	110/137	0.13	85/186	0.14
31	1,2,3,4,5	6	72/205	0.3	42/178	0.04	48/223	0.065	41/254	0.06

^a Samples S04, S06, S07, and S10 are each represented by 31 combinations. Volume V_I represents the volume of the smaller pores of the two pore systems symbolized by I and II. F_{MIP} is calculated from the data presented in Table 3. See text for further details.

Moreover, the surface area of the segment L —displayed in Figure 3—can be expressed by

$$S = \int_{\gamma} 2\pi R ds \quad (9)$$

where γ defines the curve along the surface of the cylinder in the vertical plane. This integral can be solved to give

$$S = 4L(R_0 + \Delta) \frac{1}{\sqrt{1 - \alpha^2}} E(\alpha^2, \pi/2) \quad (10)$$

where $\alpha^2 = \Delta^2 \pi^2 / (L^2 + \Delta^2 \pi^2)$ and $E(\alpha^2, \pi/2) = \int_0^{\pi/2} \sqrt{1 - \alpha^2 \sin^2 x} dx \approx (\pi/2)[a_0 + a_1 \alpha + a_2 \alpha^2]$. $E(\alpha^2, \pi/2)$ represents the elliptic integral of the second kind, i.e., with $a_0 = 1$, $a_1 = 0.094 \pm 0.012$, and $a_2 = 0.434 \pm 0.014$. The maximum relative error in this latter approximation is less than 2%.

From the above consideration it follows that the volume ratio of two pore volumes V_I and V_{II} determined by MIP, $(V_I/V_{II})_{MIP}$, can be related to the corresponding volume ratio obtained by NMR, $(V_I/V_{II})_{NMR}$, by

$$\left(\frac{V_I}{V_{II}}\right)_{MIP} = \frac{1 + 2\frac{\Delta_2}{R_{2,MIP}} + 3\left(\frac{\Delta_2}{R_{2,MIP}}\right)^2}{1 + 2\frac{\Delta_1}{R_{1,MIP}} + 3\left(\frac{\Delta_1}{R_{1,MIP}}\right)^2} \left(\frac{V_I}{V_{II}}\right)_{NMR} \quad (11)$$

The relative volume ratio $F_V = V_{MIP}/V_{NMR}$ and the relative surface ratio $F_S = S_{NMR}/S_{MIP}$ of the perturbed (NMR) and nonperturbed (MIP) pore geometry are depicted in Figure 4 as a function of pore radius (R) for different values of the

perturbation amplitude, Δ ($= 1, 5, 10$, and 15 \AA) with L being a constant equal to 10 \AA . In the small pore region the pore volume of the perturbed geometry, shows up to 40% larger volume than the unperturbed geometry while the perturbed surface area shows more than 7 times larger area compared to the unperturbed geometry.

If comparing the volume ratio $(V_I/V_{II})_{NMR}$ of two different pore systems I and II—with pore dimensions R_I and R_{II} ($R_I < R_{II}$)—and assuming $0 < \Delta < 20 \text{ \AA}$, we see from eq 11 and the data in Table 4 that $0 < \Delta_{II}/R_{II} < 0.16$ and $0 < \Delta_I/R_I < 0.36$, which implies

$$0.52(V_I/V_{II})_{NMR} < (V_I/V_{II})_{MIP} < 1.36(V_I/V_{II})_{NMR} \quad (12)$$

From the calculated 95% confidence interval of the $(V_I/V_{II})_{NMR}$ ratio (Table 3), the corresponding 95% confidence interval of the expected $(V_I/V_{II})_{MIP}$ ratio can be estimated from eq 12. The results are summarized in Table 5.

Pore Dimension and Volume Ratio of Contracted Pores.

From the above discussion we can define some relevant criteria in order to reduce the number of acceptable two-pore combinations presented in Table 4. Considering the 95% confidence interval of the MIP volume ratios (Table 5)—as derived from NMR measurements—we can easily select the pore systems (Table 4) that have observed MIP volume ratios within the estimated confidence region. These systems are assigned with an asterisk in Table 4 and reveal four systems of sample S04, one system of sample S06, seven systems of sample S07, and 15 systems of sample S10.

A further reduction of the number of two-pore combinations can be made by applying eq 5. If assuming (1) $1/T_{1s} \gg 1/T_{1b}$ (which will be verified later in this work) and (2) the pores to

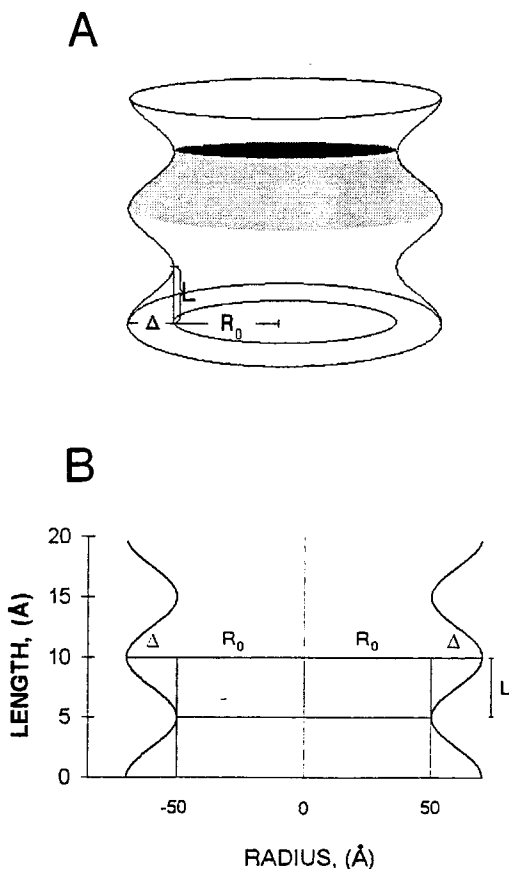


Figure 3. Three-dimensional (A) and two-dimensional (B) picture of a pore as described by a cosine perturbed pore model (eq 7). R_0 is the radius measured by MIP, Δ is the amplitude of perturbation, and L represents the half-width of the pore opening.

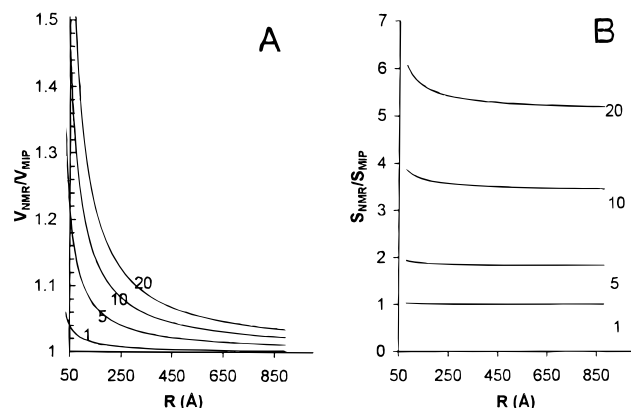


Figure 4. (A) Relative volume ratio, $V_{\text{NMR}}/V_{\text{MIP}}$, and (B) surface ratio, $S_{\text{NMR}}/S_{\text{MIP}}$, vs pore radius (R_{MIP}) for different values of the perturbation amplitude Δ ($\Delta = 1, 5, 10$, and 15 \AA). L is constant and equal to 10 \AA .

TABLE 5: Expected MIP Volume Ratio (V_I/V_{II})_{MIP} as Derived from the NMR Volume Ratio (V_I/V_{II})_{NMR} by Applying Eq 12; The Tabulated Values Represent 95% Confidence Intervals

sample	$(V_I/V_{II})_{\text{MIP}}$
S04	3.6–22.7
S06	0.56–2.56
S07	0.45–1.51
S10	0.16–2.52

be cylindrical, eq 5 simplifies to $T_{\text{II}}/T_{\text{III}} \approx R_I/R_{\text{II}}$. Thus, considering the significant difference in spin–lattice relaxation times of the two pore systems of sample S04 of 1.50 and 8.48 s, respectively, we would expect the ratio R_I/R_{II} to fall in the range 2.8–11.5. On the basis of this observation system 19,

21, and 24 can be excluded from further analysis, resulting in only a single two-pore system (system 1) of sample S04. The same argument can be applied to samples S07 and S10 resulting in exclusion of systems 3, 5, and 9 and systems 1, 2, 5, 7, 14, and 17, respectively.

The total number of possible two-pore combinations are thus reduced from 923 521 ($31 \times 31 \times 31 \times 31$) to 36 ($1 \times 1 \times 4 \times 9$). Taking into account the uncertainty in pore radius derived from MIP analysis, the following two-pore systems of sample S10 cannot be considered significantly different: systems (4, 8, 11), (9, 12, 23), and (18, 20). In Table 6 these systems are represented by their respective average pore radii.

To find a single solution among the remaining 16 ($=1 \times 1 \times 4 \times 4$) combinations (Table 6), the following model calculation is performed.

Model Calculation. The thickness (λ) of the surface water layer has been the subject of intense debate for many decades.^{13,14} However, there seems to be a general agreement that this layer covers only a few monolayers of water molecules. Hansen and co-workers¹⁵ determined this thickness from NMR analysis of the freezing of water confined in mesoporous MCM-41 materials and found $\lambda = 3.51 \pm 0.56 \text{ \AA}$, which corresponds to one to two monolayers of water molecules. Other researchers in the field have published similar results.^{16,17} The parameter $2L$, which represents the maximum pore opening of the perturbed pores along the cylindrical pore surface, must be small enough to make the MIP technique insensitive to this dimension. We have chosen $2L = 10 \text{ \AA}$, which represents pore sizes in the microporous range. To determine the perturbation amplitude Δ_i for each of the eight pore sizes (corresponding to the two pore sizes for each of the four samples S04–S10), eq 4 is applied where V and S are expressed by eqs 8a and 10, respectively. An initial guess of the eight Δ_i values and the surface spin–lattice relaxation rate, $1/T_{\text{IS}}$, are made in order to calculate the eight initial spin–lattice relaxation rates ($1/T_{\text{I,calc}}$) from eq 5. The least-squares sum $S = \sum (1/T_{\text{I,obs}} - 1/T_{\text{I,calc}})^2$ has been minimized by applying a simplex algorithm with the constraint $\sum \Delta_i^2 = \text{minimum}$. This latter constraint has been chosen in order to minimize the perturbation amplitude and, more important, to obtain a unique, single solution to our problem. This procedure has been applied to all 16 possible pore combinations (Table 6), and the one giving the least value of S has been chosen as the specific solution to our problem. The results are shown in Table 6, resulting in $1/T_{\text{IS}} = (2.27 \pm 0.12) \times 10^3 \text{ s}^{-1}$, which corresponds to a surface spin–lattice relaxation time $T_{\text{IS}} = 441 \pm 23 \text{ \mu s}$. This rather short spin–lattice relaxation time is not surprising for water molecules located at a surface, due to the reduced mobility of the molecules. Using the value $\lambda = 3.5 \text{ \AA}$, the surface interaction parameter λ/T_{IS} can be calculated and amounts to $(0.793 \pm 0.042) \times 10^{-4} \text{ cm/s}$, which is in excellent agreement with the value $(0.5\text{--}1.25) \times 10^{-4} \text{ cm/s}$ reported by Bhattacharja et al.⁵ on porous silica. The Δ_i values are shown in Table 7 together with the calculated volume ratios ($V_{\text{NMR}}/V_{\text{MIP}}$) for each pore size. All volume ratios are systematically larger than or equal to 1, indicating that the volumes derived from MIP are somewhat smaller than the corresponding volumes derived from NMR. This observation has been previously related to the inherent “blindness” or insensitivity of detecting pore dimensions in the microporous range by MIP. Figure 5 shows the perfectly linear relation between $1/T_1$ and surface-to-volume ratio (S/V) when applying the perturbed cylindrical pore model in contrast to the simple cylindrical pore model, which shows a decreasing change in predicted S/V ratio with increasing spin–lattice relaxation rate or decreasing pore radius. For small pore radii (large spin–

TABLE 6: Possible Pore Combinations Consistent with NMR and MIP Pore Volume Ratios^a

remaining pore combinations	S04		S06		S07		S10		S10	
	R_I (Å)	R_{II} (Å)	R_I (Å)	R_{II} (Å)	R_I (Å)	R_{II} (Å)	R_I (Å)	R_{II} (Å)	S	$1/T_{IS} \times 10^{-3}$ (s ⁻¹)
A	135	1197	106	478	116	737	108	543	1.07	2252
B	135	1197	106	478	116	737	103	361	1.10	2148
C	135	1197	106	478	116	737	110	241	1.58	1578
D	135	1197	106	478	116	737	83	261	1.42	1709
E	135	1197	106	478	112	254	108	543	1.02	2185
F	135	1197	106	478	112	254	103	361	1.30	1767
G	135	1197	106	478	112	254	110	241	1.33	1709
H	135	1197	106	478	112	254	83	261	1.29	1731
I	135	1197	106	478	55	215	108	543	1.16	1850
J	135	1197	106	478	55	215	103	361	1.12	1850
K	135	1197	106	478	55	215	110	241	1.69	1313
L	135	1197	106	478	55	215	83	261	1.19	1724
M	135	1197	106	478	90	468	108	543	1.00	2252
N	135	1197	106	478	90	468	103	361	1.03	2148
O	135	1197	106	478	90	468	110	241	2.47	1029
P	135	1197	106	478	90	468	83	261	1.28	1727

^a S represents the least-squares sum of the observed and calculated relaxation rates (see text for further details) where S for system M is set arbitrarily to 1. $1/T_{IS}$ represents the surface spin–lattice relaxation rate derived for each pore combination A–P.

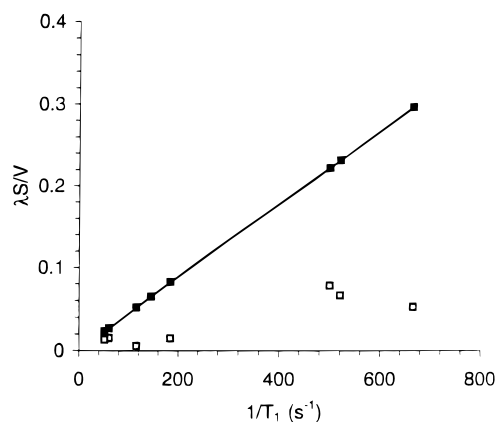


Figure 5. $\lambda S/V$ vs spin–lattice relaxation rate ($1/T_1$) obtained by a combined use of NMR and MIP by applying a pure cylindrical pore geometry (\square) and a perturbed cylindrical pore geometry (\blacksquare). λ is the thickness of the surface layer, S is the pore surface area, and V is the pore volume. The solid line represents a least-squares fit to the perturbed cylindrical pore geometry data.

TABLE 7: Derived Geometrical Perturbation Parameters (Δ_i), Surface-to-Volume Ratio ($\lambda S/V$), and the Pore Volume Ratio Obtained from MIP and NMR (V_{NMR}/V_{MIP}) (See Text for Further Details)

sample	radius (Å)	Δ (Å)	V_{NMR}/V_{MIP}	$\lambda S/V$
S04	135	14.0 ± 1.7	1.241 ± 0.057	0.293 ± 0.055
S04	1197	22.4 ± 5.0	1.029 ± 0.005	0.042 ± 0.006
S06	106	8.7 ± 0.6	1.145 ± 0.011	0.202 ± 0.013
S06	478	13.6 ± 1.1	1.050 ± 0.002	0.071 ± 0.003
S07	90	6.8 ± 0.5	1.137 ± 0.009	0.191 ± 0.013
S07	468	3.2 ± 0.3	1.013 ± 0.002	0.023 ± 0.002
S10	108	0 ± 0	1.00 ± 0.00	0.055 ± 0.003
S10	543	3.1 ± 0.4	1.013 ± 0.001	0.020 ± 0.002

lattice relaxation rates), the latter model predicts a S/V ratio of only 14% compared to the perturbed cylindrical pore model.

Uncertainties in Parameters Derived by Model Fit. To estimate the uncertainty in the parameters T_{IS} , Δ , $\lambda S/V$, and V_{NMR}/V_{MIP} , the error, $\epsilon(T_1)$, in T_1 is assumed to be normally distributed about its mean value, with a standard deviation given by σ (see Table 2). This means that a “synthetic” set of eight T_{1i} ($i = 1-8$) relaxation times, represented by an eight-dimensional vector $\vec{T} = (T_{11}, T_{12}, T_{13}, T_{14}, T_{15}, T_{16}, T_{17}, T_{18})$ can be generated for each set of eight pore sizes or pore volumes (see Table 2) where $T_{1i} = T_{1i,obs} + \epsilon_i(T_{1i,obs})$ for $i = 1-8$. Ten such sets of \vec{T} vectors have been generated and used to calculate the T_{IS} , Δ , $\lambda S/V$, and V_{NMR}/V_{MIP} parameters for each set by the

procedure outlined in the previous section. The average value and uncertainty in T_{IS} , Δ , $\lambda S/V$, and V_{NMR}/V_{MIP} have been determined by standard statistical procedure. The results are summarized in Table 7.

The relative perturbation amplitude (Δ/R) decreases with increasing pore dimension R from approximately 10% for the small pores to less than 3% for the larger pores. One exception is the pore with dimension $R = 108$ Å, which reveals a pure cylindrical pore shape. The uncertainty in the perturbation amplitude (Δ_i) is less than 10%.

Also, the volumes obtained by NMR are systematically and significantly larger than the volumes obtained by MIP by 10–24% for the smaller pore dimensions. This difference gets smaller and approaches 0 for the larger pores. This is rationalized according to the lack of sensitivity in detecting micropores by MIP.

Of particular interest is the perfect linear relation obtained between the spin–lattice relaxation rate and $\lambda S/V$ obtained by the perturbed cylindrical pore model (Figure 5), suggesting that the total surface area (S) of the porous material can be determined if the volume (V) and the thickness of the surface water layer (λ) are known. This will be discussed in the next section.

Specific Surface Area. The linear relation between $1/T_1$ and surface-to-volume ratio (S/V) makes it possible to determine the specific surface areas (S) of the cement pastes from knowledge of the total pore volume (V). The specific surface area in m²/g of hydrated cement paste dried at 105 °C is calculated to be between 236 m²/g for $w/c = 0.40$ and 127 m²/g for $w/c = 1.0$. The contribution to the specific surface area from each of the two pore systems (I and II) as well as the total surface area of samples S04, S06, S07, and S10 are shown in Table 8. The results are in rather good agreement with specific surface areas measured by water vapor adsorption¹⁸ of about 200 m²/g cement paste in the w/c ratio range from 0.35 to 0.70. Nitrogen adsorption (BET) measurements on bottle hydrated cement pastes ($w/c = \infty$)¹⁹ show values varying from 70 to 250 m²/g compared to ignited (at 1050 °C) weight obtained with different drying techniques. Low-angle X-ray measurements on hydrated cement pastes with $w/c = 0.40$ show similar results for dried samples.

Conclusion

Analysis of the mercury intrusion data of the four cement pastes investigated in this work signifies a distribution of pore

TABLE 8: Specific Surface Areas with Standard Deviation in m²/g of Hydrated Cement Paste Dried to Constant Weight at 105 °C; Both Areas Corresponding to the Contribution from Each of the Pore System Components, *S*, and Total Areas, *S*_{total}, Are Shown

sample	pore system	<i>S</i>	<i>S</i> _{total(I+II)}
S04	I	232 ± 3.0	236 ± 3.1
S04	II	3.39 ± 0.44	
S06	I	200 ± 5.9	248 ± 6.2
S06	II	47.6 ± 1.8	
S07	I	200 ± 4.6	252 ± 4.6
S07	II	52.3 ± 1.0	
S10	I	95.3 ± 4.3	127 ± 4.7
S10	II	31.4 ± 1.8	

sizes which are approximated by a sum of Gaussian functions, each of which is centered at a specific pore radius. In contrast, the NMR spin–lattice relaxation data can only be separated into two relaxation times for each sample.

An analysis of ¹H NMR spin–lattice relaxation time and pore size determined by mercury intrusion shows an underestimate of the pore volume as measured by MIP.

A modified cylindrical pore model rationalizes the observed differences in NMR and MIP volumes and gives an excellent linear correlation between the spin–lattice relaxation rate, 1/*T*₁, and surface-to-volume ratio, *S*/*V*.

The spin–lattice relaxation time of the water layer near the pore wall, *T*_{1s}, is determined as 441 ± 23 μs, giving a surface interaction parameter of (0.793 ± 0.042) 10^{−4} cm/s, which is in agreement with values found in the literature. The specific surface areas are determined to be between 127 ± 4.7 and 236 ± 3.1 m²/g, which are representative of hydrated cement pastes.

In general, once the relation between spin–lattice relaxation rate and *S*/*V* ratio is established by a combined use of MIP and NMR, the *S*/*V* ratio can be obtained from a single NMR spin–lattice relaxation time measurement on the confined water of similar materials.

Considering other types of porous materials with different surface properties (for instance different wettabilities), fluids other than water can be used to advantage to establish the above-mentioned relation.

Appendix

Small pores (micropores) are modeled by introducing a perturbation of the cylindrical pore wall by a cosine function of the form

$$R = R_0 + \Delta \left[1 + \cos\left(\frac{\pi z}{L}\right) \right] \quad (\text{A1})$$

where *R*₀ represents the radius of the unperturbed cylindrical surface, i.e., the radius determined from MIP. *L* is the half-width of the pore opening, and Δ is the amplitude of the perturbation. This is illustrated schematically in Figure 3, which shows a two-dimensional and a three-dimensional picture of the pore. We will assume that the length (*H*_{*i*}) of pore *i* is much longer than the pore radius, i.e., *H*_{*i*} ≫ *R*₀. The volume of one segment of the perturbation, *V*_L^P, is illustrated by the shaded area of Figure 3 and is expressed by the following integral (when first rearranging eq A1):

$$V_L^P = \int_{\Omega} \int_{xy\pi} \frac{L}{\pi} \arccos \left[\frac{\sqrt{x^2 + y^2} - R_0}{\Delta} - 1 \right] dx dy \quad (\text{A2})$$

where Ω defines the region in the *xy*-plane enclosed by the circles *R* = *R*₀ + Δ and *R*₀. By introducing cylindrical coordinates *x* = *R* cos θ and *y* = *R* sin θ, eq A2 can be

rearranged to give

$$V_L^P = \frac{L}{\pi} \int_{R_0}^{R_0+\Delta} \int_0^{2\pi} R \arccos \left[\frac{R - R_0}{\Delta} - 1 \right] dR d\theta \quad (\text{A3})$$

This integral can be easily solved by introducing a new variable:

$$\Phi = \arccos \left[\frac{R - R_0}{\Delta} - 1 \right]$$

with *dR* = −Δ sin Φ *dΦ*. Inserting this variable into eq A3, gives

$$V_L^P = \frac{\Delta L}{\pi} \int_0^{\pi} \int_0^{2\pi} \Phi (R_0 + \Delta + \Delta \cos \Phi) \sin \Phi d\Phi d\theta \quad (\text{A4})$$

which can be easily solved by simple calculus and gives

$$V_L^P = \frac{1}{2} \pi \Delta L (4R_0 + 3\Delta) \quad (\text{A5})$$

The total volume *V*_L of the segment is thus given by the sum of the unperturbed cylinder volume *V*_L^U (=π*R*₀²*L*) and the perturbed volume *V*_L^P, i.e.,

$$V_L = \pi R_0^2 L + \frac{1}{2} \pi \Delta L (4R_0 + 3\Delta) \quad (\text{A6})$$

which can be measured by NMR. The first term in eq A6 defines the volume of a cylinder of radius *R*₀, which is determined by MIP. We can thus define an average radius (*R*_{NMR}) of the perturbed cylindrical pore by equating volume *V*_L with the corresponding volume of a cylinder of radius *R*_{NMR} and height *L*, which gives

$$R_{\text{NMR}}^2 = R_0^2 + \frac{1}{2} \Delta (4R_0 + 3\Delta) \quad (\text{A7})$$

Moreover, the surface area of the segment *L*—displayed in Figure 4—can be determined and is given by eq A8:

$$S = \int_{\gamma} 2\pi R ds \quad (\text{A8})$$

where γ defines the curve along the surface of the perturbed cylinder, with *ds* = √*dr*² + *dz*². Expressing *R* as a function of *z* (eq A1) and introducing a new variable *u* defined by *u* = *z*π/*L*, eq A8 can be written

$$S = 2L \int_0^{\pi} (R_0 + \Delta) \sqrt{1 + \left(\frac{\Delta\pi}{L}\right)^2 \sin^2 u} du + 2L \int_0^{\pi} \cos u \sqrt{1 + \left(\frac{\Delta\pi}{L}\right)^2 \sin^2 u} du \quad (\text{A9})$$

The second integral in eq A9 is equal to zero, as can be seen from simple symmetry arguments. Introducing a parameter α defined by α² = Δ²π²/(*L*² + Δ²π²) and substituting *u* = π/(2 − *x*), the first term in eq A9 can be written

$$\begin{aligned} \int_0^{\pi} \sqrt{1 + \left(\frac{\Delta\pi}{L}\right)^2 \sin^2 u} du &= \\ \frac{1}{\sqrt{1 - \alpha^2}} \int_{-\pi/2}^{\pi/2} \sqrt{1 - \alpha^2 \sin^2 x} dx &= \\ \frac{2}{\sqrt{1 - \alpha^2}} \int_0^{\pi/2} \sqrt{1 - \alpha^2 \sin^2 x} dx \end{aligned}$$

which inserted into eq A9 gives

$$S = 4L(R_0 + \Delta) \frac{1}{\sqrt{1 - \alpha^2}} \int_0^{\pi/2} \sqrt{1 - \alpha^2 \sin^2 x} \, dx \quad (\text{A10})$$

where the integral function $\int_0^{\pi/2} \sqrt{1 - \alpha^2 \sin^2 x} \, dx$ represents the complete elliptic integral of the second kind, which is generally denoted $E(\alpha^2, \pi/2)$. We have approximated this integral by a second-order polynomial, eq A11:

$$E(\alpha^2, \pi/2) = \int_0^{\pi/2} \sqrt{1 - \alpha^2 \sin^2 x} \, dx \approx \frac{\pi}{2} [a_0 + a_1 \alpha + a_2 \alpha^2] \quad (\text{A11})$$

with $a_0 = 1$, $a_1 = 0.0937 \pm 0.012$, and $a_2 = 0.434 \pm 0.014$. The maximum relative error in this approximation is less than 2%. We see that if $\Delta = 0$, then $\alpha = 0$ and (A10) simplifies to $S = 2\pi R_0 L$, which is identical with the area of a cylinder of radius R_0 and height L , as expected.

From the above considerations it is easy to show that the volume ratio of two pore systems V_I and V_{II} obtained by MIP can be related to the corresponding volume ratio obtained by NMR by the following relation:

$$\left(\frac{V_I}{V_{II}} \right)_{\text{MIP}} = \frac{R_{1,\text{MIP}}^2 R_{2,\text{MIP}}^2 + (1/2) \Delta_{II} (4R_{2,\text{MIP}} + 3\Delta_{II})}{R_{2,\text{MIP}}^2 R_{1,\text{MIP}}^2 + (1/2) \Delta_I (4R_{1,\text{MIP}} + 3\Delta_I)} \left(\frac{V_I}{V_{II}} \right)_{\text{NMR}} \quad (\text{A12})$$

which can be transformed into eq 11.

References and Notes

- (1) Gladden, L. F. *Trans IChemE*, **1993**, 71, Part A, 657–674.
- (2) Cohen, M. H.; Mendelson, K. S. *J. Appl. Phys.* **1982**, 53 (2), 1127–1134.
- (3) D'Orazio, T.; J. C., Halperin, W. P.; Eguchi, K.; Mizusaki, T. *J. Appl. Phys.* **1989**, 65 (2), 742–751.
- (4) Gallegos, D. P.; Munn, K.; Smith, D. M.; Stermer, D. L. *J. Colloid Interface Sci.* **1987**, 119, 127.
- (5) Gallegos, D. P.; Smith, D. M. *J. Colloid Interface Sci.* **1988**, 122 (1), 143–153.
- (6) Bhattacharja, S.; Moukawa, M.; D'Orazio, F.; Jehng, J.; Halperin, W. P. *Adv. Cem. Based Mater.* **1993**, 1, 67–76.
- (7) Schreiner, L. J.; Mactavish, J. C.; Miljković, L.; Pintar, M. M.; Blinc, R.; Lahajnar, G.; Reeves, L. W. *J. Am. Ceram. Soc.* **1985**, 68, 10–16.
- (8) Lea, F. M. *The Chemistry of Cement and Concrete*, 3rd ed.; Edward Arnold Publisher Ltd.: London, 1983.
- (9) Washburn, E. W. *Proc. Natl. Acad. Sci.* **1921**, 7 (6), 3105–3114.
- (10) (a) Winslow, D. S.; Diamond, S. *J. Mater.* **1970**, 5, 564–585. (b) Kaplan, W. *Advanced Calculus*; Addison-Wesley: Reading, MA, 1971.
- (11) Halperin, W. P.; Jehng, J.-Y.; Song, Y.-Q. *Magn. Reson. Imag.* **1994**, 12, 169.
- (12) Zimmermann, J. R.; Brittin, W. E. *J. Phys. Chem.* **1957**, 61, 1328–1333.
- (13) Clifford, J. In *Water, A Comprehensive Treatise*; Franks, F., Ed.; Plenum Press: New York, 1975; Vol. 5, Chapter 2.
- (14) Packer, K. J. *Philos. Trans. R. Soc., London, B* **1977**, 278, 59.
- (15) Schmidt, R.; Hansen, E. W.; Stöcker, M.; Akporiaye, D.; Ellestad, O. H., *J. Am. Chem. Soc.* **1995**, 117, 4049–4056.
- (16) Pearson, R. T.; Derbyshire, W. J. *Colloid Interface Sci.* **1974**, 46, 232–248.
- (17) Overloop, K.; Van Gerven, L. *J. Magn. Reson. Ser. A* **1993**, 101, 179–187.
- (18) Mikhail, R. Sh.; Copeland, L. E.; Brunauer, S. *Can. J. Chem.* **1964**, 42, 426–437.
- (19) Litvan, G. G. *Cem. Concr. Res.* **1976**, 6, 139–144.